metals

Article

The Preparation and Optoelectronic Properties of Symmetric and Asymmetric Multilayered Transparent Conductive Films with ZnS-TiO_2-Ag Material System

Kai Tao [1,2,*], Hanbin Chen [3], Fangzi Zhao [1], Shiqi Li [1] and Zhiyong Liu [4]

[1] School of Materials Science and Engineering, Henan Institute of Technology, Xinxiang 453003, China
[2] Engineering Research Center for Metallic Materials Modification Technology of Henan Province, Henan Institute of Technology, Xinxiang 453003, China
[3] Southwest Technology and Engineering Research Institute, Chongqing 401329, China
[4] National Materials Corrosion and Protection Scientific Data Center, University of Science and Technology Beijing, Beijing 100083, China
* Correspondence: taokai@hait.edu.cn

Abstract

Flexible transparent conductive films with symmetric and asymmetric multilayered structures are studied using the ZnS–TiO_2–Ag material system, in order to capitalize on the divergent properties of the two dielectric layers for improved performance. The dielectric/metal/dielectric-structured films were deposited by magnetron sputtering sequentially, with high-purity targets. Multilayered films with various dielectric combinations and metallic layer thicknesses were prepared and analyzed. The surface morphology and phase structure were characterized by atomic force microscopy and scanning electronic microscopy. The optical properties were tested by spectrophotometry and analyzed by numerical simulation approach. The sheet resistance was measured via a four-point probe tester. Among the series of multilayers, asymmetric ZnS/Ag/TiO_2 film with 35 nm thickness of dielectric layers and 8.5 nm of metallic layer possesses the optimum comprehensive optoelectronic performance. The average light transmittance reaches 90.72% in the visible spectrum, and the sheet resistance is 7.69 Ω/sq. The good result is ascribed primarily to the combined advantages of superior percolation effect of bottom ZnS layer on ultrathin Ag layer, beneficial impingement effect of top layer deposition on the metallic layer, and excellent surface smoothness of the top dielectric layer.

Keywords: transparent conductive film; dielectric/metal/dielectric; asymmetric; magnetron sputtering; surface morphology; optoelectronic property

Check for updates

Academic Editor: Renato Altobelli Antunes

Received: 22 July 2026
Revised: 11 August 2026
Accepted: 18 August 2026
Published: 20 August 2026

Copyright: © 2026 by the authors. Licensee MDPI, Basel, Switzerland. This article is an open access article distributed under the terms and conditions of the Creative Commons Attribution (CC BY) license.

1. Introduction

Transparent conductive films (TCFs) play an important role as electrodes in the fields of photovoltaic devices, flat panels, light-emitting diodes, electromagnetic screens, low-emissivity glasses, etc. [1–3]. Nowadays, Indium Tin Oxide (ITO) still dominates the application of TCFs; however, the inadequacy of indium reserves and lack of flexibility of ITO films restrict further development in the flexible electronic industry. Numerous indium-free TCF materials are studied as ITO candidates, such as transparent conductive oxides of Aluminum-doped Zinc Oxide (AZO), Fluorine-doped Tin Oxide (FTO), Gallium-doped Zinc Oxide (GZO), and composite films with carbon nanotubes, graphene, silver nanowires, metallic grids, etc. [4,5]. Among the new types of TCFs, the ultrathin metallic

layer based composite films with a dielectric/metal/dielectric (D/M/D) structure have revealed excellent properties in aspects of light transmission, electrical conductivity, surface smoothness and mechanical flexibility [4,6]. Great expectations have been placed on it as one of the emerging transparent electrode materials, especially in the application of flexible electronic devices [7].

The metallic layer mainly contributes to the electrical conductivity of the D/M/D multilayer, the typical thickness of which is 6~16 nm [1,8,9], corresponding to various metal types and deposition processes. Due to the superior ductility of metallic materials, the multilayer can maintain its prime function, even with cracks under excessive deformation [5,10]. Ag possesses superb light transmittance among metals and has been adopted as the intermediate layer material for many multilayer systems [11,12].

The dielectric layers function primarily as anti-reflection and protection films on the bottom and top sides of the multilayers, further suppressing the local surface plasmon resonance (LSPR) effect in some cases [13–15] for better optical transmission properties. The multilayer structure can be symmetric, with one dielectric material on both sides, or asymmetric, with different dielectrics. ZnS is a widely used dielectric material, possessing a high refractive index and good light transmission properties [16]. It also demonstrates superior percolation properties for the intermediate metallic layer, which promotes the formation of a continuous and uniform layer at a minimal thickness [17,18], while improving film stability [18,19]. TiO_2, as another popular dielectric material, demonstrates not only excellent dielectric and optical properties, but also chemical stability, moisture resistance and photocatalytic activity [20].

Various physical vapor deposition methods have been reported to deposit TCFs with D/M/D structures, mainly with processes of vacuum evaporation, e-beam-assisted evaporation [21,22] and magnetron sputtering [8,20]. The magnetron sputtering process can provide much higher energy to the atoms or particles from the targets compared to the evaporation method. Thus, films deposited via magnetron sputtering usually exhibit denser microstructure and higher bonding force, which could obviously promote the engineering application.

The research on D/M/D multilayered TCFs has been concentrated on the symmetric structures in recent years; however, adoption of different dielectrics in the composite film was less frequently reported. The magnetron-sputtered multilayered TCFs of ZnS-TiO_2-Ag material system were prepared and analyzed in this paper, including multilayered structure combinations with ZnS and TiO_2 as the bottom or top layer, attempting to synergistically exploit the superior percolation effect of bottom ZnS layer on ultrathin Ag layer, beneficial impingement effect of top layer deposition on the metallic layer, and excellent surface smoothness of the top dielectric layer.

2. Materials and Methods

Flexible transparent polyethylene terephthalate (PET) sheets, with dimensions of $20 \times 20 \times 0.175$ mm, were adopted as substrate for the film samples. Before being fixed onto the base plate for deposition, the substrate was sequentially ultrasonic-cleaned in acetone, ethyl alcohol and deionized water for 10 min, respectively, followed by dying with high-purity N_2 gas. The sputtering targets ($\geq$99.99 purity, 76.2 mm diameter, from ZhongNuo Advanced Material (Beijing, China) Technology Co., Ltd.) of ZnS, TiO_2 and Ag were used as raw materials. A magnetron sputtering instrument (JiashuoJSD-500, Hefei, China) was utilized for depositing the various layers, equipped with 4 target positions and 4 separate sputtering power supplies. The base pressure was controlled at 5×10^{-4} Pa, and the working pressure was set to be 0.4 Pa by inflating with high-purity Ar gas. The ZnS and TiO_2 targets were matched with radiofrequency (RF) power, and the Ag target with

direct-current (DC) power. The power values for ZnS, TiO_2 and Ag were 110 W, 150 W and 90 W, respectively. The deposition rate of each layer was obtained by preparing a relatively thick (around 350 nm) layer under the identical process parameters to the corresponding multilayer fabrication, then calculating the rate via the thickness measured by white light interferometry (Rtec R-wlafm, San Jose, CA, USA) and deposition duration. The calculated rates are 0.138 nm/s for ZnS, 0.032 nm/s for TiO_2 and 0.521 nm/s for Ag. When preparing the multilayered film samples, each sublayer was sputter-deposited sequentially according to the specific structure, without breaking the vacuum state in between.

The surface morphology of each film sample was characterized by atomic force microscopy (AFM, Bruker Dimension Icon, Boston, MA, USA) and scanning electronic microscopy (SEM, Hitachi SU8010, Tokyo Japan). The quantitative measurement was conducted based on the images via the software Image J (version 1.54p). The electrical properties were measured via a four-point probe tester (Jingge M-3, Suzhou, China), and the relative optical transmittance of films was tested by spectrophotometry (Youke UV756, Shanghai, China, wavelength range 190~1100 nm). The average transmittance (T_{av}) was calculated as Equation (1):

$$T_{av} = \frac{1}{n}\sum_{i=1}^{n} T_i \tag{1}$$

where T_i represents the transmittance at a specific wavelength, and n is the number of data in defined spectrum.

The transmission spectrum data from two relatively thick (around 350 nm) dielectric films of ZnS and TiO_2, respectively, were utilized to deduce the refractive index and extinction coefficient according to the envelope approach of transmittance data [23]. These samples were deposited on electronic soda-lime glass substrates (20 × 20 × 1.1 mm) to avoid possible influence from the smoothing layer [24,25] of the PET substrates. The prime equations [23] are listed as follows:

$$N = 2s\,(T_M - T_m)/(T_M\,T_m\,) + \left(s^2 + 1\right)/2 \tag{2}$$

$$n = \left[N + \left(N^2 - s^2\right)^{1/2}\right]^{1/2} \tag{3}$$

$$T_i = \frac{2T_M T_m}{T_M + T_m} \tag{4}$$

$$F = \frac{8n^2 s}{T_i} \tag{5}$$

$$x = \frac{F - \left[F^2 - \left(n^2 - 1\right)^3\left(n^2 - s^4\right)\right]^{1/2}}{(n-1)^3(n - s^2)} \tag{6}$$

$$\alpha = -\frac{\ln x}{d} \tag{7}$$

$$k = \frac{\alpha\lambda}{4\pi} \tag{8}$$

where T_M and T_m are the maximum and minimum values of the transmittance at corresponding interference fringes, s is the refractive index of the substrate, n and k are the refractive index and extinction coefficient of the deposited films, respectively.

The transmission properties of the multilayered films were simulated via the software TFCalc (version 3.8), which is a well-received tool in designing and process controlling of optic films. The incident beam was set as white light perpendicular to the top surface of the films.

3. Results

3.1. The Complex Refractive Indexes of Dielectric Layers

The transmittance spectra of magnetron-sputtered individual dielectric films (around 350 nm thickness) are presented in Figure 1a,b. The refractive index and extinction coefficient of the two dielectric layers were then calculated from the transmission curves based on the data envelop approach, as shown in Figure 1c,d. The n values for both dielectrics developed in a similar pattern, rising rapidly from 350 nm to the visible spectrum and then descending slowly. The ZnS and TiO_2 layers exhibit close refractive indexes in the 400~800 nm spectrum, and the n values at 550 nm are 2.28 and 2.31, respectively. Whereas the extinction coefficient values differ obviously. Although the values of both materials exhibit the trend of decreasing dramatically from the ultraviolet region to visible spectrum and then tending to become stable, the ZnS layer possesses much higher k values than TiO_2, with 0.0205 and 0.0016 at 550 nm wavelength, respectively. This means the ZnS dielectric layer will intrinsically attenuate the transmittance of the multilayers compared with TiO_2.

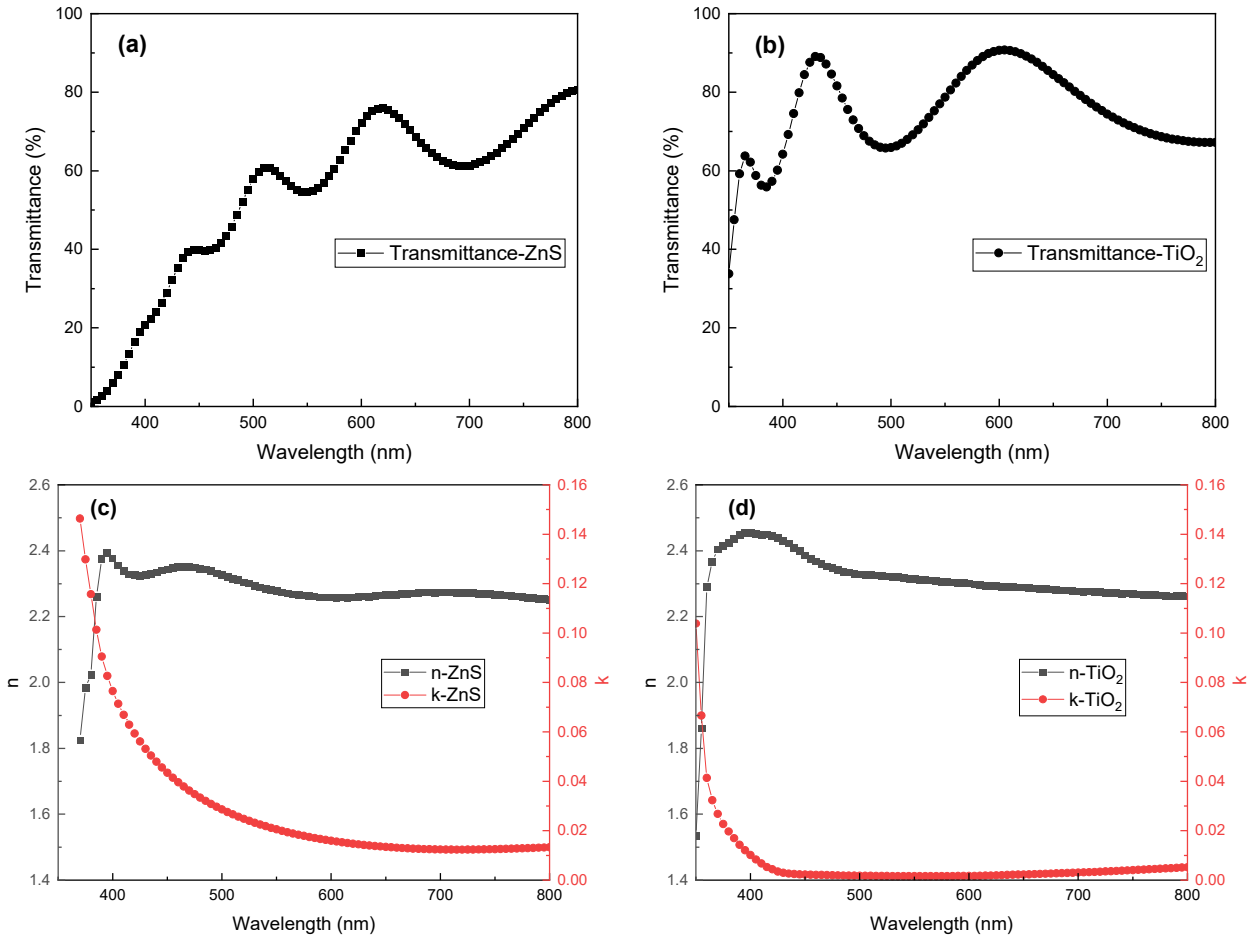


Figure 1. The transmittance spectra of magnetron-sputtered individual dielectric films: (**a**) ZnS and (**b**) TiO_2. The calculated refractive indexes (n) and extinction coefficients (k) of dielectric films: (**c**) ZnS and (**d**) TiO_2.

3.2. The Optical Transmission Properties of Multilayered TCFs

Based on the previous research results of our group [26,27], and due to the similar refractive indexes of ZnS and TiO_2 in the visible spectrum, the thickness of both dielectric layers was set to be 35 nm for all the multilayer structure combinations in this study. The TCF samples were categorized into three groups, with the respective invariant as intermediate metallic layer thickness or dielectric type, as displayed in Figure 2. The

transmission spectra of all multilayered TCF samples demonstrate typical wave-shaped curves, which is believed to arise from the interference fringes of the smoothing coating on the surface of PET substrate [24,25]. The sublayer codes were set as Z35, T35 and A8.5~11.5, which denote the layers of ZnS, TiO_2 and Ag with thicknesses of 35 nm and 8.5~11.5 nm, respectively.

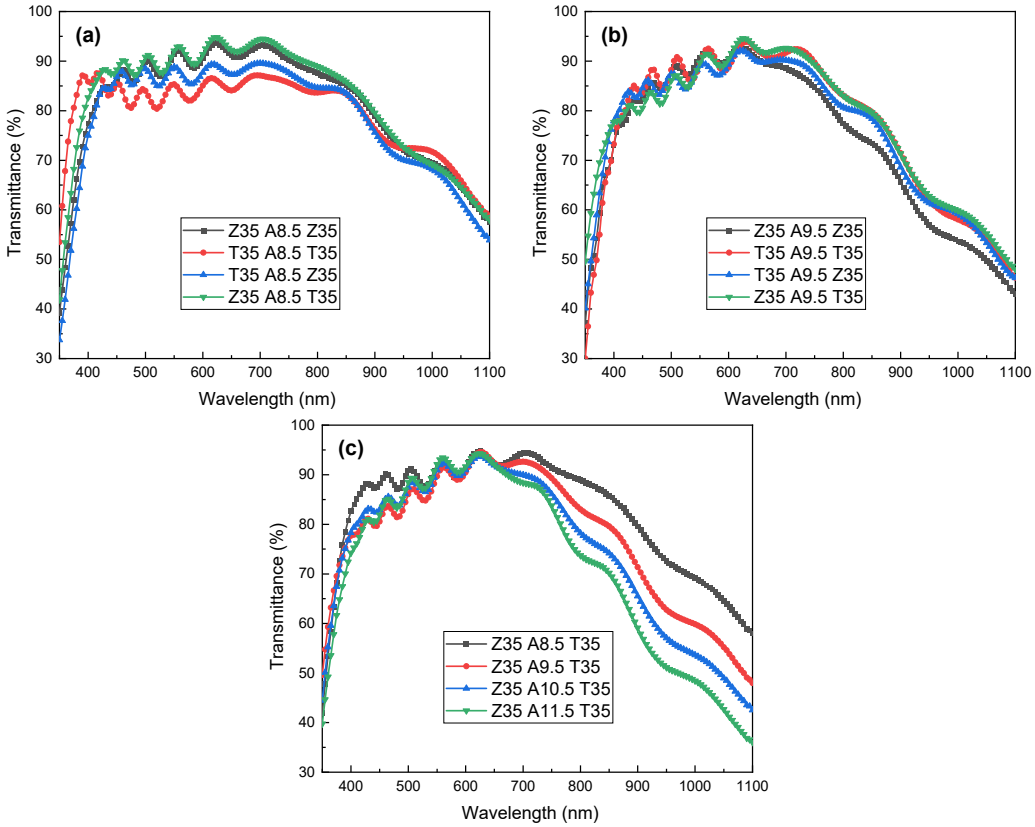


Figure 2. The light transmission spectra of TCF samples with various multilayered structures: (**a**) the group of 35 nm ZnS—35 nm TiO_2—8.5 nm Ag; (**b**) the group of 35 nm ZnS—35 nm TiO_2—9.5 nm Ag; and (**c**) the group of 35 nm ZnS—35 nm TiO_2—8.5~11.5 nm Ag.

In the first TCF group, the intermediate Ag layer was fixed to be 8.5 nm, and the transmission spectra of film samples are exhibited in Figure 2a, with different dielectric structures in the light wavelength range of 350~1100 nm. The four samples of this group share a similar trend for the transmission development, where the transmittance increases rapidly from the ultraviolet range to the visible spectrum, followed by gradually ascending to the peak value around 600 nm wavelength, then descends continually towards the infrared region. The T35 A8.5 T35 sample presents the lowest transmittance among the group counterparts, with the average transmittance in the 400~800 nm spectrum ($T_{av(400–800)}$) of 84.58%. The Z35 A8.5 T35 sample with ZnS as the bottom layer and TiO_2 as the top layer displays the best transmission properties in the visible spectrum, the $T_{av(400–800)}$ of which is 90.72%. The detailed data are listed Table 1.

Table 1. The optical and electrical properties of ZnS-TiO_2-Ag multilayered samples.

TCF	R_S (Ω/sq)	T_{550} (%)	$T_{av(400–800)}$ (%)	$\phi_{TC(550)}$ (10^{-3} Ω^{-1})	$\phi_{TC(400–800)}$ (10^{-3} Ω^{-1})
Z35 A8.5 Z35	8.17	91.47	89.22	50.18	39.12
T35 A8.5 T35	10.93	85.33	84.58	18.72	17.14
T35 A8.5 Z35	8.76	88.80	86.72	34.80	27.46
Z35 A8.5 T35	7.69	92.10	90.72	57.10	49.10
Z35 A9.5 Z35	5.60	90.60	86.43	66.54	41.54
T35 A9.5 T35	6.29	89.50	88.27	52.43	45.65
T35 A9.5 Z35	6.90	89.10	86.85	45.70	35.39
Z35 A9.5 T35	7.20	89.68	87.64	46.73	37.13
Z35 A10.5 T35	5.96	90.92	87.32	64.77	43.24
Z35 A11.5 T35	4.74	92.10	86.43	92.64	49.08

The intermediate Ag layer thickness is increased to 9.5 nm in the second sample group. These four samples possess very close transmission spectra in the entire measuring scope. The transmittances of samples reach the peak values around 650 nm wavelength. As shown in Table 1, the T35 A9.5 T35 sample possesses the optimal $T_{av(400–800)}$ value of 88.27%, and the Z35 A9.5 Z35 sample presents the minimum average value of 86.43%. Comparing the patterns in Figure 2a, it is found that the transmittance curves here decline more pronouncedly from around 700 nm wavelength to the infrared region. This is a representative phenomenon arising from the strengthened light reflection and absorption effect of thicker and more continuous Ag layers. However, the 1 nm thickness increase in Ag layer does not bring the uniform change on the transmittances of the four structures. The $T_{av(400–800)}$ decreases by about 3% for the Z/A/Z and Z/A/T structures, while the value increases by about 4% for the T/A/T structure and maintains stable for the T/A/Z sample.

Since the Z35 A8.5 T35 sample demonstrates the best transmittance result in the visible spectrum, we expanded the intermediate layer thickness range to explore the optical characteristics of asymmetric Z/A/T structures, as seen in Figure 2c. The sample with the thinnest 8.5 nm Ag layer presents the highest transmittance, covering the measuring spectrum from 350 to 1100 nm. With the increase in the Ag thickness, the transmission properties generally display a descending trend in the visible region, as the $T_{av(400–800)}$ value changes in Table 1. Furthermore, the decreasing trend of transmittance starts to intensify close to the infrared spectrum, which is again ascribed to the thickening effect of Ag layers, as discussed in Figure 2b.

3.3. The Electrical Conductivity of Multilayered TCFs

The sheet resistances (R_s) of multilayered samples with different structures are illustrated in Figure 3, and the detailed data are listed in Table 1. In the first sample group with 8.5 nm thickness Ag layer, the T/A/T-structured sample exhibits the highest R_s of 10.93 Ω/sq, while the Z/A/T one possesses the lowest value of 7.69 Ω/sq. It is interesting to note that the performance ranks on both electrical conductivity and optical transmission are consistent for this group of samples.

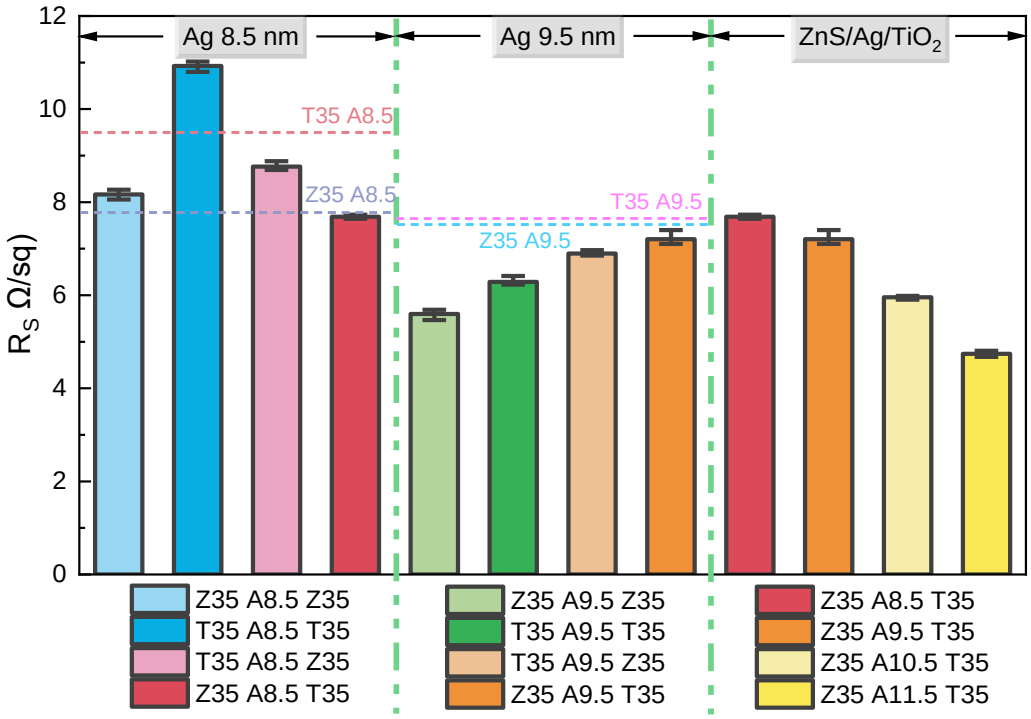


Figure 3. The sheet resistance of ZnS-TiO_2-Ag multilayered samples with different structures.

With the metallic layer thickness increasing to 9.5 nm, the electrical conductivities of the entire group of samples have improved obviously. Among the four structures, the T/A/T sample displays the most distinct decrease on the sheet resistance, and ranks the second in the group, whereas the Z/A/T one falls to the last position. The Z/A/Z sample here shows the best electrical conductivity with the sheet resistance of 5.60 Ω/sq.

For the Z/A/T-structured samples in the third group, the sheet resistance decreases stably with the growth of Ag thickness, as expected. The intermediate metallic layer plays the dominant role for the electrical conductivity for the D/M/D-structured TCF. Thicker Ag layer thickness means more continuous state and corresponding more carrier concentration with higher Hall mobility [28]. The sample with 11.5 nm thickness Ag layer presents the lowest sheet resistance, of 4.74 Ω/sq, among all the samples in this paper.

3.4. Morphology Characterization

3.4.1. The Surface Morphology of the Dielectric Layer

Due to the limited electrical conductivity of the dielectric materials, AFM method was adopted for the surface morphology characterization of ZnS and TiO_2 layers. The single ZnS and TiO_2 layers with thickness of 35 nm were deposited under the identical process parameters as corresponding D/M/D films. The AFM images are displayed in Figure 4. The average surface roughness of ZnS layer is Ra 0.387 nm, and Ra 0.400 nm for TiO_2. Both types of dielectric layers demonstrate fair smoothness as the bottom layer of the D/M/D structure, which would facilitate the optical and electrical performance of the multilayered films [24].

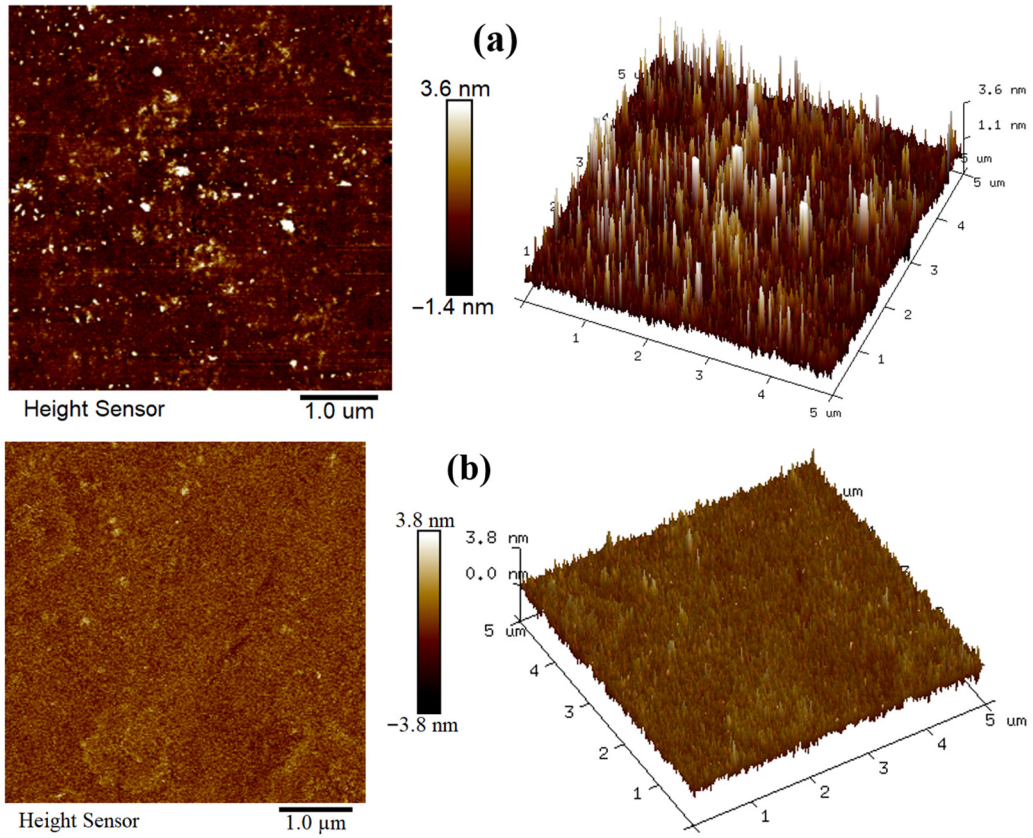


Figure 4. AFM images of the surface morphology of dielectric layers: (**a**) ZnS; (**b**) TiO_2.

3.4.2. The Surface Morphologies of Multilayered Films

During the sequential sputtering of multilayered samples, the films acquired good electrical conductivity since the intermediate metallic layer deposition. Thus, the surface morphology of the metallic layer and top dielectric layer could be characterized by SEM method, which is relatively more efficient.

The surface morphologies of Ag layers with different thicknesses and bottom layers are shown in Figure 5. On the bottom layer of ZnS, Ag layer can form almost continuous film at the small thickness of 8.5 nm, where the uncovered area is only 0.11%. There are a few relatively big particles of light color, with an average size of about 40 nm, as seen in Figure 5a. When the Ag layer thickness reaches 9.5 nm, a fully continuous metallic film is obtained. This layer seems more uniform compared to the previous one, with some rock-shaped particles of a smaller average size around 35 nm.

When considering the ones with TiO_2 bottom layer, the morphology differs evidently from the former ZnS samples. With 8.5 nm thickness Ag layer, the sample surface presents more uncovered areas, shown as the irregular dark patterns in Figure 5c. The uncovered area percentage reaches 3.28%, and a number of relatively large particles of light color are randomly distributed, with an average size of about 70 nm. With the metallic layer thickness reaching 9.5 nm, the uncovered area percentage slumps to 0.36%. The surface morphology is denser and more homogeneous, with a small number of large particles having an average size of around 55 nm.

The surface morphology of top dielectric layers from different multilayered structures is displayed in Figure 6. The surface of top ZnS layer in Z/A/Z structure, shown in Figure 6a, exhibits a continuous, uniform and smooth state, comprising small, round-shaped particles with an average size of about 28 nm. The other symmetric T/A/T structure presented a much different surface morphology, as displayed in Figure 6b. The

surface of the TiO_2 layer consists of relatively large particles with a wide range of size distribution, which exhibits an obviously ununiform and rough state. There are a few large particles in spherical shape, with an average size of around 93 nm. The particles appear a light color under the second electronic mode of SEM analysis, mainly due to the geometric features.

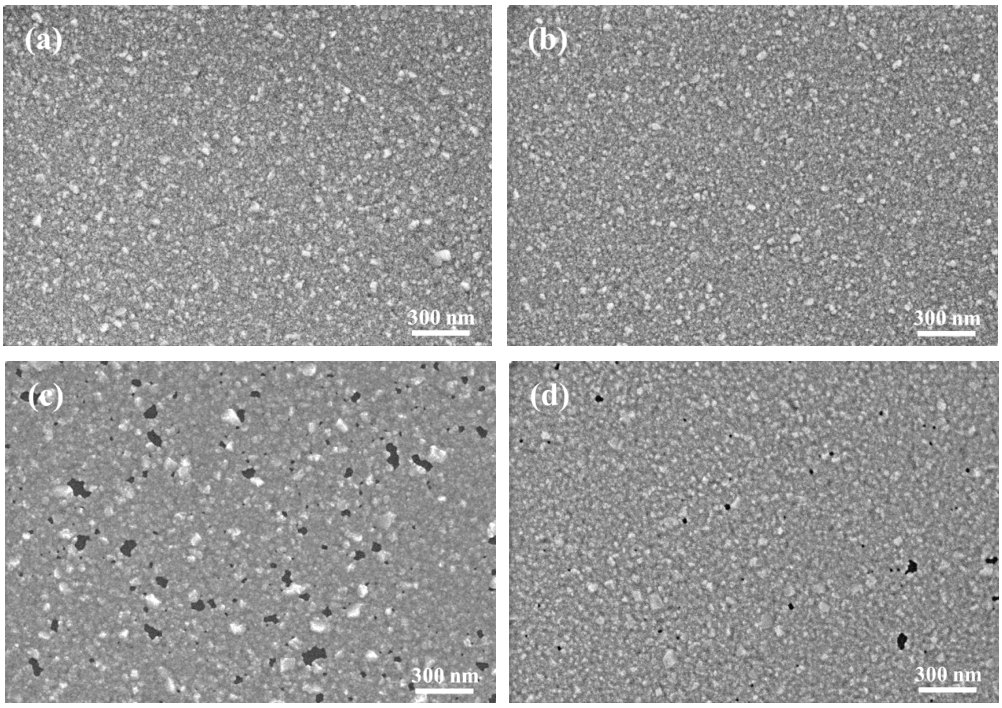


Figure 5. The SEM images of Ag layer morphology with different thicknesses and bottom layers: (**a**) Z35 A8.5; (**b**) Z35 A9.5; (**c**) T35 A8.5; and (**d**) T35 A9.5.

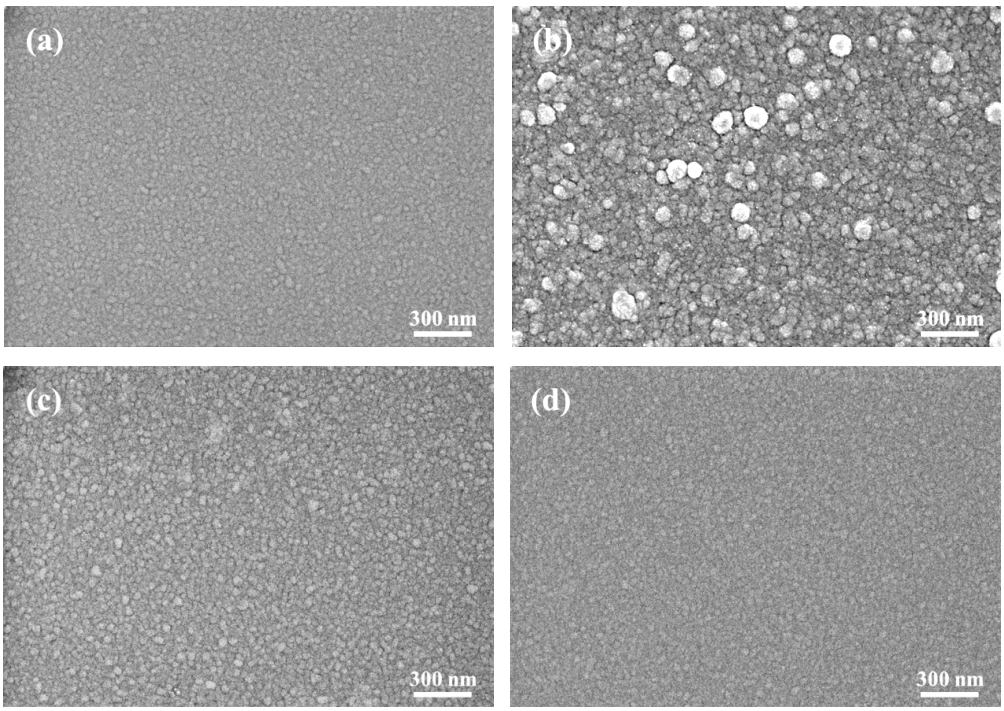


Figure 6. The SEM images of top dielectric layer morphology with different multilayered structures: (**a**) Z35 A9.5 Z35; (**b**) T35 A9.5 T35; (**c**) T35 A9.5 Z35; and (**d**) Z35 A9.5 T35.

For the asymmetric-structured samples, both the top ZnS and TiO_2 layers demonstrate different morphologies from their symmetric counterparts. The top ZnS layer in T/A/Z structure presents kind of rougher and nonuniform morphology features compared with the Z/A/Z structure, as shown in Figure 6c. The particles here possess an average size of about 30 nm, and some of them tend to agglomerate to form larger clusters. The surface morphology of Z/A/T structure exhibits the most homogeneous and smooth state among the four samples, as displayed in Figure 6d, where the particles on the surface possess an average size of around 26 nm.

4. Discussion

4.1. The Transmittance Gap Between Experimental and Simulated Results

The light transmission results of multilayered samples are not always satisfying (Table 1). To analyze the adverse factors, optical simulations were carried out via the software TFCalc, as the simulation results could be regarded as kind of an ideal state, which is based on the optical interfering mechanism of the incident and reflective lights among sublayers with perfectly regular forms. The schematic representation of the film structure for optical simulation is shown in Figure 7. The initial simulated transmittance is the absolute value, which involves the substrate in the film structure. These results were then divided by the measured transmittance values of the bare PET substrate to obtain the equivalent relative transmittance. The comparison of experimental and simulated results is demonstrated in Figure 8, grouped by the multilayered structure type. The gap values of average transmittance in the visible spectrum [21] are listed in Table 2.

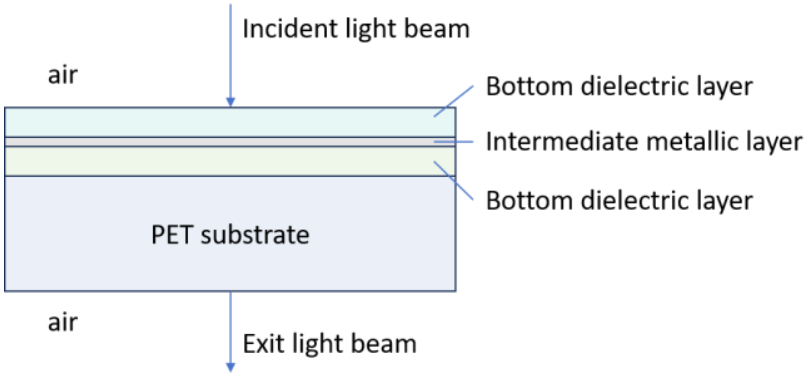


Figure 7. The schematic representation of the film structure for transmittance simulation.

Table 2. The gap of transmittance between the experimental and simulated results for TCFs with varied structures.

TCF	Z35 A8.5 Z35	T35 A8.5 T35	T35 A8.5 Z35	Z35 A8.5 T35
$\Delta T_{av(400–800)}$ (%)	−3.74	−12.44	−8.11	−4.27
TCF	Z35 A9.5 Z35	T35 A9.5 T35	T35 A9.5 Z35	Z35 A9.5 T35
$\Delta T_{av(400–800)}$ (%)	−7.02	−9.44	−8.57	−7.94
TCF	—	—	—	Z35 A10.5 T35
$\Delta T_{av(400–800)}$ (%)	—	—	—	−8.45
TCF	—	—	—	Z35 A11.5 T35
$\Delta T_{av(400–800)}$ (%)	—	—	—	−9.14

Note: $\Delta T_{av(400–800)}$ is the absolute difference value between the experimental and simulated results for the average light transmittance in the spectrum of 400–800 nm.

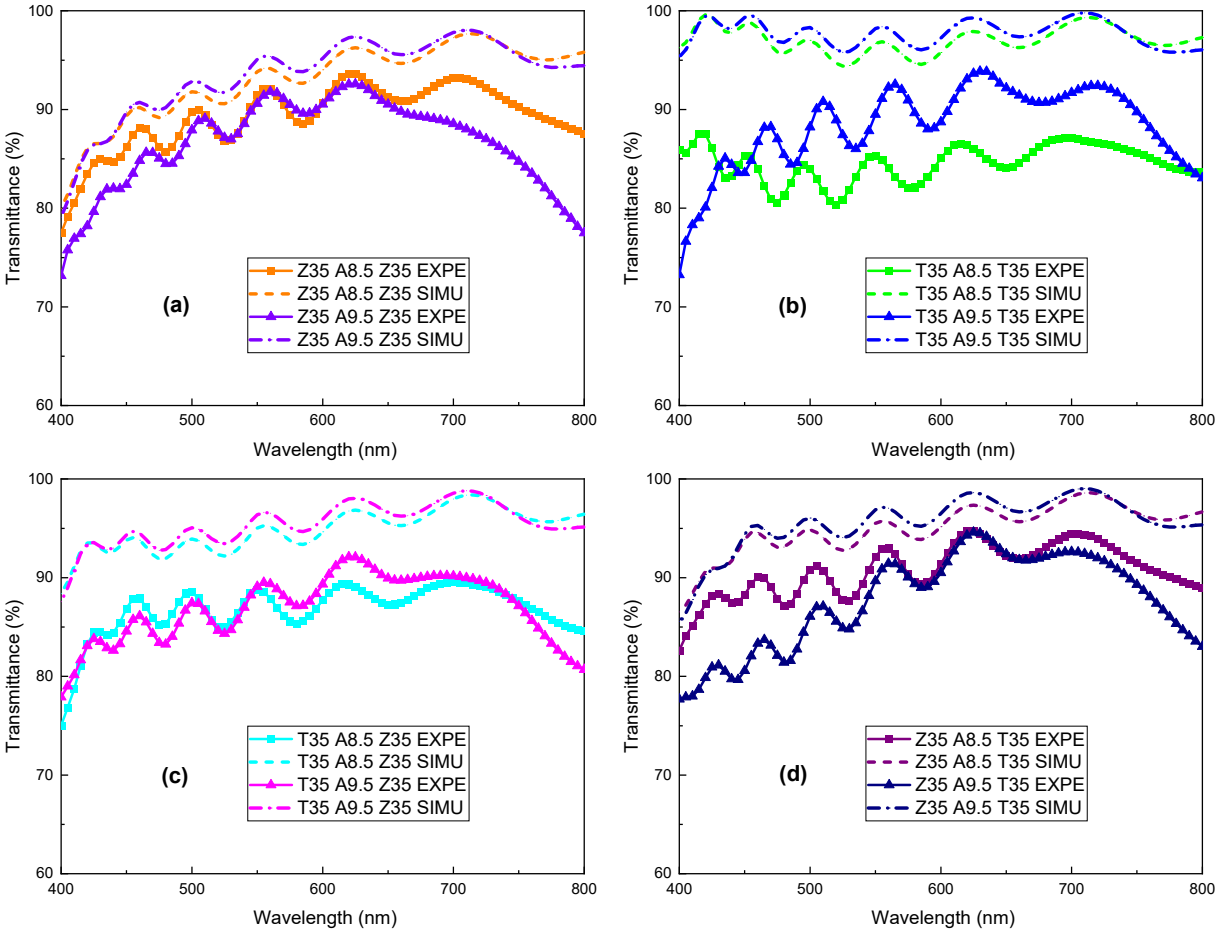


Figure 8. The transmittance curves of multilayered TCFs from experimental and simulated results. (**a**) ZnS/Ag/ZnS structure; (**b**) TiO_2/Ag/TiO_2 structure; (**c**) TiO_2/Ag/ZnS structure; (**d**) ZnS/Ag/TiO_2 structure.

The transmittance gap for Z/A/Z structures is generally the smallest among the four structures, which increases with the thickness growth of intermediate layer. ZnS, as the bottom layer, demonstrates superior percolation property, which facilitates the formation of continuous and smooth metallic layer at a thinner thickness compared to TiO_2 (shown in Figure 2). This advantage effectively suppresses the incident light loss of scattering or LSPR effect from discontinuous layer. The gap values of the T/A/T structures are the largest among the four types. The maximum difference occurs at the T35 A8.5 T35 sample, then diminishes with the thickening of metallic layer.

For the multilayers with TiO_2 bottom layer, adopting the ZnS layer on top improves the overall transmission property of the TCFs with 8.5 nm Ag layer, compared with the symmetric structure. When the Ag layer increases to 9.5 nm thickness, the gap value remains nearly stable.

For the Z/A/T structure, the transmittance gap is close to the Z/A/Z group. The change in top dielectric layer does not evidently influence the transmittance feature, which again indicates the substantial interface improvement of the bottom ZnS layer. With the growth of metallic layer from 8.5 to 10.5 nm thickness, the Z/A/T structure keeps a monotonically increasing trend, as shown in the last column of Table 2. It should to be attributed primarily to the variation in actual ultrathin Ag layer morphology and interfacial state, which deviate from the ideal situation in the multilayers. Although the sputtered ZnS layer has a relatively higher extinctive coefficient (shown in Figure 1), the better interface

situation of the bottom layer enhances the overall optical properties of the asymmetric multilayered film, especially with thinner metallic layer.

4.2. The Effect of Different Multilayered Structures on Electrical Conductivity

In the D/M/D structure, the resistance of metallic layer is far lower than that of dielectric layer; therefore, the intermediate metallic layer plays the dominant role for the electrical conductivity of multilayers. In an ideal situation, the samples in this study with the identical metallic layer parameters should possess the same sheet resistance. However, differently structured samples present varied results. To better analyze the electrical properties, the bilayer films with D/M structure are also marked on corresponding groups in Figure 3, as the initial state of the electroconductivity (Z35 A8.5—7.54 Ω/sq, T35 A8.5—9.06 Ω/sq, Z35 A9.5—7.04 Ω/sq, T35 A9.5—7.23 Ω/sq). Due to the excellent percolation property of ZnS layer, Ag layer is significantly more continuous at the lower thickness (8.5 nm). Thus Z/A structure presents better electrical conductivity in the first group. When the thickness increases to 9.5 nm, The Ag layer tends to be fully continuous on both types of bottom layers, which diminishes the conductivity difference. The above phenomena correspond well to the SEM results shown in Figure 2.

In the conditions of 8.5 nm Ag layer, the two D/M/D-structured samples with bottom ZnS layer demonstrate close sheet resistance to the D/M structure. Nevertheless, the R_S values of the other two D/M/D samples with bottom TiO_2 layer deviate from their bilayer counterparts, where the top layer of ZnS lowers the resistance, while TiO_2 does the opposite. In the situation of 9.5 nm Ag layer, all of the complete D/M/D-structured samples possess a smaller R_S value than their respective bilayer counterparts. Furthermore, both symmetric-structured samples reveal smaller R_S values than the other asymmetric ones. The ranking sequence in the former group of 8.5 nm metallic layer totally changed in the latter one, indicating that the effects of different multilayered structures on the electrical conductivity vary with the parameters of metallic layer. Since the resistance of a continuous metallic layer is mainly ascribed to the diffuse scattering of the conductive electrons at the surfaces, interfaces, grain boundaries, and other defects [29,30], these microstructural characteristics of different multilayered structures are diverse from each other.

4.3. The Effects of Multilayered Structures on Optoelectrical Properties

In the optical aspect, the sputtered single TiO_2 layer presents better light transmission properties, on account of its lower extinction coefficient, than ZnS. According to the simulation results, TiO_2-involved multilayers should possess preferable transmittances. However, the optical performances of films also depend strongly on other factors, like the surface or interface morphology features and material microstructures. In the simulation of light transmission, the deduced complex refractive indexes of the dielectrics were adopted as the material data, to take into consideration the specific process effects on the optical properties. Even so, the numerical simulation via the software is based on the presumption that each sublayer possesses a perfectly continuous and smooth form. Therefore, there is a difference between the simulated and experimental results. This gap is primarily ascribed to the state of intermediate metallic layer, as it has an ultrathin thickness and good plasticity, which means it is easy to change its initial state during sputtering deposition of the top dielectric layer. With respect to the electrical properties, the sheet resistance deviations of the D/M/D-structured samples from the D/M structures also indicate the significant influence of the top layer on the metallic layer performance. The samples with bottom ZnS layer generally demonstrate positive effects of the top layer deposition, whereas the samples with bottom TiO_2 layer present different effects of top layer deposition, depending on the material type, sputtering power and metallic layer thickness.

The Haacke's Figure of Merit ($\phi_{TC} = T^{10}/R_S$) [31] is adopted here to denote the comprehensive optoelectrical properties of the multilayered TCFs, as listed in Table 1. The numbers at wavelength of 550 nm are also displayed for reference, which are not as representative as the average values because of the wave-like shape of the transmission spectrum on the PET substrate. In the first group of samples with 8.5 nm thickness of Ag layer, the Z35 A8.5 T35 possesses the highest transmittance and the lowest conductivity; therefore, it possesses the best Figure of Merit ($49.10 \times 10^{-3}\ \Omega^{-1}$) in the visible spectrum. In the second sample group, with 9.5 nm thickness of metallic layer, the two symmetrically structured samples demonstrate better $\phi_{TC(400–800)}$ than both the asymmetric ones, mainly due to their superior conductivity. In the last group, owing to the continuous growth of Ag layer thickness, the transmission and conductivity properties develop in opposite directions. The $\phi_{TC(400–800)}$ of this structure shows favorable values at the 8.5 nm and 10.5 nm of Ag layer thickness, indicating suitable structure parameters. This result is close to that of L. Peres. [21], where the Z/A/T-structured TCF fabricated by e-beam evaporation method demonstrates a maximum $\phi_{TC(400–800)}$ of $42.5 \times 10^{-3}\ \Omega^{-1}$. In this study, due to the much higher energy of deposited atoms derived from the magnetron-sputtering process [32], the intermediate metallic layer tends to suffer significant impingement during the deposition of top dielectric layer. Therefore, the final state of the intermediate layer probably changes evidently from the initial state, maybe denser, smoother and more continuous, or the opposite, as demonstrated of the R_S results in Figure 4.

Additionally, the different crystallization states of bottom layer may also affect the microstructure (including interfacial coherent type, crystallization state, grain size, etc.) of intermediate layer and even the top layer [33]. This phenomenon probably corresponds to the different morphologies for the top layer of the same dielectric but with different bottom layer materials, as displayed in Figure 3.

The TiO_2 layer, as the top layer, exhibits significant difference in morphology between the TiO_2/Ag/TiO_2 and ZnS/Ag/TiO_2 structures, and the latter presents the best smoothness of top surface among the four multilayer structures. The bottom ZnS layer contributes excellent percolation properties to facilitate the formation of continuous and smooth Ag layer at a low thickness [34]. Furthermore, taking into account the optimized optical structure parameters and the impingement effects of the top layer deposition, Z35 A8.5 T35 structure demonstrates the best comprehensive optoelectrical performance among all ten D/M/D-structured TCF samples in this study.

5. Conclusions

Flexible transparent conductive films of ZnS-TiO_2-Ag material system were prepared via magnetron sputtering and characterized, with respective symmetric and asymmetric D/M/D structures.

The Ag layer forms a continuous and uniform film at 8.5 nm thickness on bottom ZnS layer, which demonstrates better percolation properties than TiO_2. The asymmetric ZnS/Ag/TiO_2 structure possesses the smoothest and most uniform surface morphology among the four dielectric-layer combinations (ZnS/Ag/ZnS, TiO_2/Ag/TiO_2, TiO_2/Ag/ZnS and ZnS/Ag/TiO_2).

The average transmittance of the multilayers in visible spectrum generally tends to descend with the increase in Ag layer thickness, except the T/A/T structure presents obviously higher values with 9.5 nm thickness of Ag layer than 8.5 nm. The Z35 A8.5 T35 film presents the highest average transmittance of 90.72% in the 400–800 nm wavelength range. The optical properties of the multilayers not only depend on the light interfering effect among sublayers, but also largely on the layer forms and morphologies of surfaces and interfaces.

https://doi.org/10.3390/met16080930

The sheet resistance of the multilayered films generally decreases with the growth of the metallic layer thickness. The Z35 A11.5 T35 sample possesses the smallest value of 4.74 Ω/sq.

The Z35 A8.5 T35 film possesses the best Haacke's Figure of Merit among the series of multilayers, with a $\phi_{TC(400–800)}$ of 49.10 × 10^{-3} Ω^{-1}. This is primarily ascribed to the combined advantages of superior percolation effect of bottom dielectric layer on intermediate layer, beneficial impingement effect of top layer deposition on metallic layer and excellent surface smoothness of the top dielectric layer.

Author Contributions: Conceptualization, K.T. and Z.L.; methodology, H.C. and K.T.; software, F.Z. and K.T.; validation, H.C. and S.L.; formal analysis, K.T. and H.C.; investigation, F.Z. and S.L.; resources, Z.L. and K.T.; data curation, F.Z. and S.L.; writing—original draft preparation, K.T.; writing—review and editing, H.C. and Z.L.; visualization, F.Z. and S.L.; supervision, Z.L.; project administration, K.T.; funding acquisition, K.T. All authors have read and agreed to the published version of the manuscript.

Funding: The study was funded by the Science and Technology Project of Henan Province (No. 232102231016).

Data Availability Statement: The original contributions presented in this study are included in the article. Further inquiries can be directed to the corresponding author.

Conflicts of Interest: Hanbin Chen was employed by the Southwest Technology and Engineering Research Institute. The remaining authors declare that the research was conducted in the absence of any commercial or financial relationships that could be construed as a potential conflict of interest.

References

1. Rabizadeh, M.; Ehsani, M.H. Effect of heat treatment on optical, electrical and thermal properties of ZnO/Cu/ZnO thin films for energy-saving application. *Ceram. Int.* **2022**, *48*, 16108–16113. [CrossRef]
2. Wu, J.; Qian, X.; Liu, C.; Ji, Y.; Yu, S. Design and realization of neutral-tinted low-E film. *Vacuum* **2022**, *203*, 111228. [CrossRef]
3. Lu, W.; Jiang, S.; Wang, P.; Yu, W.; Liu, X.; Wu, L.; Ding, W.; Fu, G. Recent progress of multilayer composite transparent conductive film. *Chin. Sci. Bull.* **2017**, *62*, 372–384. [CrossRef]
4. Girtan, M.; Negulescu, B. A review on oxide/metal/oxide thin films on flexible substrates as electrodes for organic and perovskite solar cells. *Opt. Mater. X* **2022**, *13*, 100122. [CrossRef]
5. Zhang, J.; Zhang, W.; Cheng, H.-M.; Silva, S.R.P. Critical review of recent progress of flexible perovskite solar cells. *Mater. Today* **2020**, *39*, 66–88. [CrossRef]
6. Guillén, C.; Herrero, J. TCO/metal/TCO structures for energy and flexible electronics. *Thin Solid Films* **2011**, *520*, 1–17. [CrossRef]
7. Lee, S.-M.; Koo, H.-W.; Kim, T.-W.; Kim, H.-K. Asymmetric ITO/Ag/ZTO and ZTO/Ag/ITO anodes prepared by roll-to-roll sputtering for flexible organic light-emitting diodes. *Surf. Coat. Technol.* **2018**, *343*, 115–120. [CrossRef]
8. Zhao, G.; Tan, Y.; Wang, B.; Jeong, E.; Zhang, L.; Wang, T.; Yu, H.; Min, G.; Han, S.Z.; Sun, Y.; et al. Understanding the role of engineered cluster evolution in enhancing Ag layer growth on oxides. *Appl. Surf. Sci.* **2024**, *644*, 158745. [CrossRef]
9. Illhwan, L.; Jong-Lam, L. Transparent electrode of nanoscale metal film for optoelectronic devices. *J. Photonics Energy* **2015**, *5*, 057609. [CrossRef]
10. Jiang, S.; Wei, Y.; Liu, H.; Lu, W.; Yu, W. Research Progress of Flexible Organic/Inorganic Hybrid Perovskite Solar Cells. *Chin. J. Lumin.* **2018**, *39*, 1687–1696. [CrossRef]
11. Huang, L.-J.; Zhang, G.-M.; Zhang, Y.; Li, B.-J.; Ren, N.-F.; Zhao, L.; Wang, Y.-L. Preparation and Photoelectric Properties of Patterned Ag Nanoparticles on FTO/Glass Substrate by Laser Etching and Driving Layer Strategy. *Acta Metall. Sin. (Engl. Lett.)* **2021**, *34*, 973–985. [CrossRef]
12. Zhu, H.; Zhang, Y.; Zhao, L.; Nie, L.; Liu, J. Preparation of Ag-based transparent conductive films with high figure-of-merit from dielectric layers' combination. *Opt. Quantum Electron.* **2024**, *57*, 40. [CrossRef]
13. Wang, S.; Nian, Y.; Wang, Y.; Lu, C.; Li, H.; Chu, X.; Qi, F.; Ma, P.; Fang, Y. Optimization on the performance of dielectric/silver/dielectric flexible transparent electrodes by variation of the chemical states of Cu seed layer. *Vacuum* **2026**, *245*, 114959. [CrossRef]
14. Jin, J.; Liu, C.; Yang, Z.-j.; Wang, L. The influence of AZO films on morphology and surface plasmon resonance properties of Ag particles. *Surf. Coat. Technol.* **2019**, *363*, 135–141. [CrossRef]

15. Maniyara, R.A.; Rodrigo, D.; Yu, R.; Canet-Ferrer, J.; Ghosh, D.S.; Yongsunthon, R.; Baker, D.E.; Rezikyan, A.; García de Abajo, F.J.; Pruneri, V. Tunable plasmons in ultrathin metal films. *Nat. Photonics* **2019**, *13*, 328–333. [CrossRef]
16. Chen, Z.; Huang, J.; Chen, Z.; Hu, Y.; Li, H.; Zhang, R.; Tang, K.; Wang, L. Influence of Cu Thickness and Annealing on the Properties of ZnS/Cu/ZnS Multilayer Films. *J. Electron. Mater.* **2020**, *49*, 4498–4503. [CrossRef]
17. Feng, W.; Zhao, G.; Li, Z.; Li, J.; Ji, F.; Zhang, R.; Liu, X.; Chen, T.; Wang, T.; Zhang, L.; et al. ZnS-enabled ultrathin Ag layers with high transparency and conductivity for flexible optoelectronic devices. *Vacuum* **2025**, *241*, 114630. [CrossRef]
18. Kim, D.-Y.; Han, Y.C.; Kim, H.C.; Jeong, E.G.; Choi, K.C. Highly Transparent and Flexible Organic Light-Emitting Diodes with Structure Optimized for Anode/Cathode Multilayer Electrodes. *Adv. Funct. Mater.* **2015**, *25*, 7145–7153. [CrossRef]
19. Han, Y.C.; Lim, M.S.; Park, J.H.; Choi, K.C. ITO-free flexible organic light-emitting diode using ZnS/Ag/MoO_3 anode incorporating a quasi-perfect Ag thin film. *Org. Electron.* **2013**, *14*, 3437–3443. [CrossRef]
20. Kim, J.H.; Kim, D.-H.; Seong, T.-Y. Realization of highly transparent and low resistance TiO_2/Ag/TiO_2 conducting electrode for optoelectronic devices. *Ceram. Int.* **2015**, *41*, 3064–3068. [CrossRef]
21. Peres, L.; Bou, A.; Barakel, D.; Torchio, P. ZnS | Ag | TiO_2 multilayer electrodes with broadband transparency for thin film solar cells. *RSC Adv.* **2016**, *6*, 61057–61063. [CrossRef]
22. Amotchkina, T.; Trubetskov, M.; Hahner, D.; Pervak, V. Characterization of e-beam evaporated Ge, YbF_3, ZnS, and LaF_3 thin films for laser-oriented coatings. *Appl. Opt.* **2020**, *59*, A40–A47. [CrossRef] [PubMed]
23. Swanepoel, R. Determination of the thickness and optical constants of amorphous silicon. *J. Phys. E Sci. Instrum.* **1983**, *16*, 1214. [CrossRef]
24. Cho, H.; Yun, C.; Park, J.-W.; Yoo, S. Highly flexible organic light-emitting diodes based on ZnS/Ag/WO_3 multilayer transparent electrodes. *Org. Electron.* **2009**, *10*, 1163–1169. [CrossRef]
25. Uchihara, D.; Riki, T. Transparent Electroconductive Film and Manufacturing Method Therefor. CN103282539A, 4 September 2013.
26. Li, M.; Tao, K.; Lu, J.; Xu, S.; Sun, Y.; Chen, Y.; Liu, Z. Preparation and Properties of Flexible Multilayered Transparent Conductive Films on Substrate with High Surface Roughness. *Materials* **2025**, *18*, 3389. [CrossRef] [PubMed]
27. Li, Q.; Tao, K.; Zhang, J.; Ren, Y.; Liu, Z. Structural, Optical and Electrical Properties of the Flexible, Asymmetric TiO_2/Cu/Ag/ZnS and ZnS/Cu/Ag/TiO_2 Films Deposited via Magnetron Sputtering. *Coatings* **2025**, *15*, 650. [CrossRef]
28. Dhar, A.; Alford, T.L. High quality transparent TiO_2/Ag/TiO_2 composite electrode films deposited on flexible substrate at room temperature by sputtering. *APL Mater.* **2013**, *1*, 12102. [CrossRef]
29. Sivaramakrishnan, K.; Alford, T.L. Conduction and transmission analysis in gold nanolayers embedded in zinc oxide for flexible electronics. *Appl. Phys. Lett.* **2010**, *96*, 201109. [CrossRef]
30. Zhang, D.; Yabe, H.; Akita, E.; Wang, P.; Murakami, R.-i.; Song, X. Effect of silver evolution on conductivity and transmittance of ZnO/Ag thin films. *J. Appl. Phys.* **2011**, *109*, 104318. [CrossRef]
31. Haacke, G. New figure of merit for transparent conductors. *J. Appl. Phys.* **1976**, *47*, 4086–4089. [CrossRef]
32. Oniszczuk, A.W.; Owen, D.S.; Loch, D.A.L.; Hovsepian, P.E.; Ehiasarian, A.P. Reverse pulse strategies for silicon dioxide thin films deposition by high power impulse magnetron sputtering. *Surf. Coat. Technol.* **2025**, *505*, 132117. [CrossRef]
33. Ciambriello, L.; Cavaliere, E.; Gavioli, L. Influence of roughness, porosity and grain morphology on the optical properties of ultrathin Ag films. *Appl. Surf. Sci.* **2022**, *576*, 151885. [CrossRef]
34. Kaiser, N. Review of the fundamentals of thin-film growth. *Appl. Opt.* **2002**, *41*, 3053–3060. [CrossRef] [PubMed]

Disclaimer/Publisher's Note: The statements, opinions and data contained in all publications are solely those of the individual author(s) and contributor(s) and not of MDPI and/or the editor(s). MDPI and/or the editor(s) disclaim responsibility for any injury to people or property resulting from any ideas, methods, instructions or products referred to in the content.